13B.5 EVOLUTION OF A QUASI-LINEAR CONVECTIVE SYSTEM SAMPLED BY PHASED ARRAY RADAR

Jennifer F. Newman*
School of Meteorology, University of Oklahoma, Norman, Oklahoma

Pamela L. Heinselman
NOAA/National Severe Storms Laboratory, Norman, Oklahoma

1. INTRODUCTION

A disproportionately large fraction of violent tornadoes are spawned by supercell thunderstorms (e.g., Doswell 2001); however, a significant fraction of tornadoes are associated with squall lines or quasi-linear convective systems (QLCSs). Trapp et al. (2005) found that 18% of all tornadoes during a three-year period were caused by lines, as opposed to supercells or other phenomena such as tropical systems. Furthermore, Trapp et al. (2005) discovered a temporal bias in QLCS tornadoes. While the occurrence of both supercell and QLCS tornadoes peaked around 6 pm local time, QLCS tornado occurrence displayed a secondary peak during the late night and early morning hours, coincident with the tendency for linear storm systems to form after sunset (e.g., Maddox 1983). Since the public is less aware of severe weather warnings at night (e.g., Ashley et al. 2008), this secondary peak in QLCS tornado occurrence presents a significant risk.

Although QLCS tornadoes tend to be fairly weak, they can reach F2 intensity (Fujita 1971) and cause thousands of dollars in damage (Trapp et al. 2005). The fact that QLCS tornadoes can form in many locations along a squall line could present a challenge to forecasters trying to issue warnings. In addition, QLCS tornadoes do not typically produce a descending velocity signature on radar data (Trapp et al. 1999), an important precursor for classic supercell tornado events (Brown et al. 1978).

*Corresponding author address: Jennifer Newman, OU School of Meteorology, 120 David L. Boren Blvd., Norman, OK
E-mail: Jennifer.Newman@ou.edu

On 2 April 2010, the National Weather Radar Testbed Phased Array Radar (NWRT PAR, hereafter PAR) in Norman, Oklahoma sampled a tornadic circulation associated with a QLCS during the early morning hours. Although the event was not officially classified as a tornado by the National Weather Service (NWS), an independent survey team determined that damage in Rush Springs, Oklahoma was the result of a tornado rated EF1 on the enhanced Fujita scale (e.g., Marshall 2004). A variety of other radars also captured the event, including the Weather Surveillance Radar 1988-Doppler (WSR-88D) in Twin Lakes (KTLX), the Terminal Doppler Weather Radar (TDWR) in Oklahoma City, and the Collaborative Adaptive Sensing of the Atmosphere (CASA; Junyent et al. 2010) radar in Rush Springs (KRSP). The availability of radar data with different frequencies and resolutions allows for a unique dataset with opportunity for comparison. The location of all four radars, in addition to the approximate path of the Rush Springs tornado, is shown in Fig. 1.

This paper focuses on the evolution of the QLCS near Rush Springs as sampled by PAR. The rapid temporal updates and dense vertical sampling of the PAR data assist in depicting the damaging wind mechanisms associated with the QLCS in great detail. Comparisons will be made to the data collected by the other radars in central Oklahoma, with emphasis given to the WSR-88D data used by NWS forecasters.

2. BACKGROUND

Mesoscale convective systems (MCSs) can span 100 km or more in length and cause damaging winds and tornadoes. Hazards associated with MCSs are caused by a variety of phenomena, including bow echoes (e.g., Fujita 1978), downbursts (Fujita 1978), microbursts (Fujita 1981), and tornadoes.

A conceptual model of a bow echo is shown in Fig. 2. The bow echo development stage has been attributed to the existence of a strong rear-inflow jet (RIJ; e.g., Smull and Houze 1987), a jet that travels from the rear to the front of a QLCS. The RIJ forms when the updraft is tilted rearward over the cold pool and air is accelerated downshear. The effects of baroclinically, cold pool-generated vorticity, and vorticity generated by the updraft-induced horizontal buoyancy gradient, combine to accelerate air up and over the cold pool (Fig. 3).

Initially, damaging wind associated with bow echoes was attributed to the descent of the RIJ to the surface (e.g., Smull and Houze 1987). Detailed radar analyses and damage surveys indeed reveal large swaths of damage collocated with the RIJ in several bow echoes (e.g., Wheatley et al. 2006). However, many damage surveys have also revealed smaller, more intense areas of damage located within or outside the main damage swath (e.g., Fujita 1978, 1981; Forbes and Wakimoto 1983). Based on numerical simulations, Weisman and Trapp (2003) and Trapp and Weisman (2003) propose that meso-γ-scale vortices, or mesovortices within the bow echo are responsible for these narrow areas of damage.

Several conceptual models for mesovortex formation have been proposed based on both modeling studies (e.g., Trapp and Weisman 2003; Atkins and St. Laurent 2009b) and observational data (e.g., Wakimoto et al. 2006b). Similar to Trapp and Weisman (2003) and Wakimoto et al. (2006b), Atkins and St. Laurent (2009b) propose that the tilting and stretching of baroclinically generated vorticity is the primary cause for mesovortex formation. However, while the earlier studies attribute the tilting effect to sub-system scale downdrafts (Fig. 4), Atkins and St. Laurent (2009b) suggest that updrafts are the primary tilting mechanism. In addition, while previous studies have found vorticity couplets in association with mesovortices, Atkins and St. Laurent (2009b) examine the formation of cyclonic-only vorticity maxima. Atkins and St. Laurent (2009b) propose that these vortices form when air descending roughly parallel to the gust front acquires the horizontal vorticity induced by the leading edge of the cold pool. This horizontal vorticity is subsequently tilted and stretched by an updraft along the gust front.

Both tornadic and nontornadic mesovortices have been observed in bow echoes (e.g., Atkins et. al. 2005). Although further research is needed, Atkins et al. (2005) showed that for the 10 June 2003 Saint Louis bow echo, the tornadic mesovortices were much deeper, stronger, and longer-lived than their nontornadic counterparts. In addition, the tornadic mesovortices produced more intense damage and formed at or near the time of RIJ descent. Atkins et al. (2005) propose that the descending RIJ in their case increased low-level convergence at the location of the gust front, enhancing vorticity stretching and the likelihood for tornado formation.

3. SYNOPTIC OVERVIEW

At 0000 UTC on 2 April 2010, the evening prior to the event, a surface low pressure system was located near Nebraska. A cold front extended southward through Kansas and the Oklahoma and Texas panhandle regions, and a well-defined dry line was in place east of the cold front (Fig. 5a). Over the next twelve hours, the low weakened slightly and moved northeastward while the cold front moved eastward across western Oklahoma and Texas (Fig. 5b).

An upper-level trough started developing on 31 March 2010 off the coast of California and moved southeastward on 1 and 2 April 2010. By 1200 UTC on 2 April 2010, the trough was slightly negatively tilted and its base was located over New Mexico (Fig. 6). Downstream from the trough, a deep layer of southerly flow advected moisture from the Gulf of Mexico toward central Oklahoma. Some weak warm air advection was apparent at 500 hPa over central and southern Oklahoma. Low-level winds increased in magnitude ahead of the upper-level trough and by 1200 UTC on 2 April 2010, a 25 ms^{-1} low-level jet was located over central Oklahoma. Although the jet was not particularly strong, it supported significant, largely unidirectional low-level shear.

In the 0000 UTC 2 April 2010 sounding launched from Norman, Oklahoma ~10 hours prior to the QLCS event, an elevated mixed layer (EML) was located atop a moderately strong capping inversion (Fig. 7a). The EML was characterized by a nearly dry-adiabatic lapse rate up to ~500 hPa. By 1200 UTC, the cap had eroded and a QLCS was in progress in western Oklahoma (Fig. 7b). Based on the 1200 UTC Norman sounding, the surface-based Convective Available Potential Energy (CAPE) was 467 J kg^{-1} and the mixed-layer CAPE (MLCAPE) was 1304 J kg^{-1}. This MLCAPE value is on the lower end of expected values for MCS or bow echo environments (e.g., Weisman 1993, Evans and Doswell 2001).

By 1200 UTC, wind speeds had increased considerably in response to the approaching upper-level trough. Based on the 1200 UTC Norman, Oklahoma sounding (Fig. 7b), the magnitude of the surface to 2.5 km wind shear was approximately 20 m s^{-1}. According to a numerical modeling study by Weisman and Trapp (2003), this low-level shear value is sufficient for the formation of bow echoes and the development of strong mesovortices. In this modeling study, weaker low-level shear values were associated with scattered, disorganized cells located far behind the gust front. In the weak shear case, the baroclinic vorticity at the leading edge of the cold pool becomes stronger than the vorticity associated with the environmental shear, and the updraft is tilted strongly upshear over the cold pool. In addition, the RIJ descends behind the leading edge of convection. However, when the low-level shear is increased to a magnitude of at least 20 m s^{-1} in the lowest 2.5 km above ground level, the environmental and baroclinic vorticity are in balance; the RIJ remains elevated and initiates upright updrafts at the leading edge of the system. Weisman and Trapp (2003) found that mesovortices tended to form near bow-shaped segments of updrafts along the leading edge of the line for these moderately strong low-level shear cases. Atkins and St. Laurent (2009a) suggest that upright updrafts promote stretching of vertical vorticity, possibly leading to the genesis of mesovortices.

4. EVENT OVERVIEW

By 0230 UTC on 2 April 2010, a line of storms had formed in western Kansas and the Oklahoma panhandle as the northern portion of the cold front merged with the retreating dry line. The line moved eastward over the next three hours and had weakened significantly by the time it reached central Kansas. This line of storms was associated with several marginally severe hail reports in Kansas. In southern Oklahoma and Texas, convection was likely inhibited by a strong capping inversion at this time.

As the upper-level trough approached from the west, storms started to form further south along the cold front. Several isolated storms had formed in northwest Texas, just south of the Oklahoma border, around 0600 UTC. As these storms developed and moved eastward, they moved into a region of moderate instability. The 0800 and 0900 UTC Storm Prediction Center (SPC) mesoanalyses indicated surface-based CAPE (SBCAPE) values around 1000 J kg^{-1} in portions of Texas and southwest Oklahoma (Fig. 8). In particular, the 0900 UTC mesoanalysis indicated a region of uncapped 1000 J kg^{-1} SBCAPE in central Oklahoma, near the location of Rush Springs.

The isolated storms grew in both size and intensity as they moved into this narrow corridor of instability (Fig. 9). Between 0800 and 1000 UTC, the southern storms increased moderately in strength while more storms formed rapidly further north in Oklahoma. The storms in Texas moved northeastward into Oklahoma, forming a QLCS by 1030 UTC (Fig. 10a). Between 1055 and 1130 UTC, a bowing segment formed in the southern portion of the QLCS, causing significant wind damage in the Rush Springs area (Fig. 10b). This portion of the QLCS also produced two microbursts. The QLCS moved eastward through Oklahoma and weakened during the early morning hours.

It is likely that the environment further south was more conducive to isolated storm cells with damaging potential. In comparison to the northern portion of the affected area, the low-level moisture in southern Oklahoma and Texas was much richer (as evidenced by dewpoint temperatures in the mid- to upper-60's F in the surface analyses leading up to QLCS formation). In addition, the low-level jet in central Oklahoma and Texas was not as prevalent in Kansas. This southerly jet served to advect moisture northward into Oklahoma and increase low-level shear, enhancing the likelihood for severe thunderstorm and bow echo formation. As a result of strong low-level shear and moderate instability, the most damaging storms initially formed in southern Oklahoma.

Fig. 11 shows the SPC damage reports from the early Kansas storms and the beginning of the Oklahoma QLCS event. A damage survey of Rush Springs was led by Kiel Ortega, a research associate with the Cooperative Institute for Mesoscale Meteorological Studies. The damage survey team determined that the Rush Springs damage was the result of an EF1 tornado (see Fig. 1 for tornado path). Debris signatures included peeled roof shingles and several rolled-over mobile homes.

5. PAR DATA ANALYSIS

5.1 *Sampling Strategies*

PAR is an S-band (9.38 cm) research radar located in Norman, Oklahoma. Unlike a WSR-88D radar, the PAR operates by using a panel of transmit/receive elements, changing the phases of the elements to steer the radar beam in azimuth and elevation. Electronic beam steering offers several potential advantages over conventional mechanical steering, including a 75% reduction in volumetric scan time (compared to a WSR-88D radar) and the ability to adaptively scan regions of interest (Zrnić et al. 2007).

The transmitted beamwidth of the PAR increases gradually with increasing angle from boresight, ranging from 1.5° at boresight to 2.1° at an angle of 45° from boresight. Overlapped sampling is used, such that the azimuthal sampling interval at a particular location is equal to one half of the beamwidth at that location. The range resolution of the PAR is 240 m (Zrnić et al. 2007).

On 2 April 2010, the PAR was operating nearly continuously from 1037 to 1140 UTC. Two different scanning strategies were used to collect data. Initially, an oversampled scanning strategy was employed, which collects data at 22 elevation angles and uses a split cut waveform at the lowest elevation angles to properly place range-folded echoes. Once the QLCS had moved within 120 km of the PAR, a different scanning strategy was employed. The second scanning strategy also collected data at 22 elevation angles, but a uniform pulse repetition time (PRT) was used for all tilts, allowing for a faster update time. The average volumetric update times for the two scanning strategies were 2 min and 1.4 min, respectively. The Adaptive Data Signal Processing Algorithm for PAR Timely Scans (ADAPTS; Heinselman and Torres 2010) algorithm, developed by the National Severe Storm Laboratory, was used to further decrease update time. ADAPTS only scans active beam positions, such that regions where no weather is occurring are not scanned.

5.2 *Microburst*

The first event sampled by the PAR was a microburst ~110 km from the radar that resulted in estimated 30 m s^{-1} winds in Cotton County and knocked over several power poles (NCDC 2010). In addition, golf-ball sized hail fell in association with the microburst (NCDC 2010). Fig. 12 shows a series of PAR reflectivity cross sections from the time of the microburst. A reflectivity core elongates and descends toward the ground, where the microburst winds spread out laterally in all directions. A surface divergence signature was also noted in the velocity field at 1048 UTC (not shown). The detailed microburst evolution depicted in the PAR data is similar to the findings of Heinselman et al. (2008).

5.3 *Strengthening RIJ*

Beginning at 1049 UTC, a RIJ strengthens and begins to descend (Fig. 13). The RIJ is first seen in the PAR data around 1048 UTC at ~6 km above mean sea level (MSL) (not shown). Initially, a small area of approaching velocities is evident at midlevels; velocity magnitudes are 5–8 m s^{-1} in the outer regions of the RIJ and 10–12 m s^{-1} in the narrow RIJ core. Between 1050 and 1052 UTC (Fig. 13a,b), the RIJ core increases drastically in both strength and depth. By 1054 UTC (Fig. 13c), a large region in the RIJ exhibits storm-relative velocities exceeding 10 m s^{-1}. By 1101 UTC (Fig. 13f), most storm-relative velocities in the RIJ core are 11–14 m s^{-1}. The strengthening RIJ creates an area of convergence where it meets the front-to-rear inflow (x~35 km, z~6 km in Fig. 13e).

Effects of the strengthening RIJ were also evident in the near-surface wind field. Fig. 14 shows the spatial and temporal evolution of the RIJ as well as the development of an area of strong outflow at the 0.5° elevation angle. Between 1052 and 1058 UTC, a region of strong inbound storm-relative motion expands northwestward along the QLCS and increases in magnitude (Fig. 14a–d). This region of strong outflow is still apparent at the 0.5° elevation angle from 1058 to 1102 UTC, when the circulation was causing EF1-scale damage in Rush Springs (Fig. 14d–f).

Atkins et al. (2005) also observed an increase in near-surface outflow coincident with a strong RIJ in a bow echo system. Atkins et al. (2005) attribute the development of this strong outflow to the descent of the RIJ. Inspection of PAR velocity cross sections for the Rush Springs case suggests that the RIJ did not descend until 1106 UTC, after the circulation had caused damage (see next section). However, it is possible that the strengthening RIJ caused a downward transport of momentum, which enhanced the near-surface outflow. The effect of this downward momentum transport on the Rush Springs circulation is discussed in section 5.6.

5.4 *Descending RIJ*

At 1106 UTC, the RIJ begins to descend toward the ground behind the main area of convection (Fig. 15b). By 1109 UTC, the RIJ has reached the surface, at x~35 km in Fig. 15d. Coincident with the descent of the RIJ is a developing and descending reflectivity appendage located to the southwest of the main area of convection (to the left in Fig. 15). This reflectivity appendage could either be a developing updraft, induced by the descending RIJ, or precipitation being forced toward the ground by the RIJ. Since the reflectivity appendage never increases in strength or vertical extent, indicating the formation of a cell, it is likely that the latter of these two explanations is more likely. Soon after the RIJ descends, the reflectivity core in the main cell in Fig. 15 also descends, in what is likely a second microburst.

Although the low-level shear on 2 April 2010 was fairly significant (see synoptic overview section), the descent of the RIJ far behind the leading edge of convection suggests that this event more closely fits the weak shear case as described by Weisman and Trapp (2003). Since the RIJ descended behind the leading edge of convection and wasn't temporally associated with any damage, it is likely that the mesovortex, rather than the descending RIJ, was responsible for the majority of the wind damage in Rush Springs.

5.5 *Mesovortex circulation*

Since only a cyclonic vortex was observed in both PAR and CASA data (Mahale et al. 2010), as opposed to a vorticity couplet, it is possible that a cyclonic vortex only mesovortex genesis mechanism was taking place, as discussed in the background section (see also Atkins and St. Laurent 2009b). However, without the use of a numerical simulation or trajectory analysis, it is difficult to determine source regions for the mesovortex air parcels and the origin of the vertical vorticity associated with the mesovortex.

By 1102 UTC, a moderately strong velocity couplet (velocity difference ~ 20 m s^{-1}) associated with the mesovortex was evident in the 0.5° PAR storm-relative motion field (Fig. 16). A cross section following the path of the velocity couplet from 1052 UTC to 1104 UTC shows a low-level azimuthal shear maximum increase in vertical extent and magnitude, reaching a value of 0.0729 s^{-1} at 1100 UTC, before tilting downshear and weakening (Fig. 17). The path of the low-level shear maximum agrees well with the tornado damage path. Azimuthal shear was calculated using the local, linear least squares derivatives (LLSD) method (Smith and Elmore 2004).

The azimuthal shear cross sections suggest that the circulation is developing from the ground up, which is typical for some non-supercell tornadoes (e.g., Wakimoto and Wilson 1989), particularly those that form in association with a QLCS (Trapp et al. 1999). This ground-up development is consistent with the tornadic mesovortices studied by Atkins et al. (2005). Weisman and Trapp (2003) found that mesovortices tilted rearward with height over the cold pool in numerical simulations, likely as a result of the circulation induced by the baroclinic vorticity on the leading edge of the cold pool. This upshear tilt was also observed by Wakimoto et al. (2006b) in a Doppler wind synthesis of a developing tornadic mesovortex. The downshear tilt of the shear maximum in this case may be the result of an imbalance between the cold pool vorticity and the vorticity due to vertical wind shear. A reflectivity cross section taken along the path of the azimuthal shear maximum reveals that the updraft in the vicinity of the mesovortex appears to be tilted downshear as well.

5.6 *Enhancement of mesovortex circulation*

The strengthening of the RIJ coincides with the timing of mesovortex formation, indicated by a developing velocity couplet in the PAR data (Fig. 14). In their study of a bow echo during the BAMEX project, Atkins et al. (2005) also noted that tornadic mesovortex genesis was associated with RIJ formation and descent. Atkins et al. (2005) suggest that the RIJ can create localized areas of convergence and strengthen the gust front, increasing the likelihood for mesovortex formation. In particular, the RIJ could promote stronger vertical vorticity stretching along the gust front.

Fig. 18 compares the convergence field to the location of the RIJ from 1054 to 1101 UTC, the period when damage was occurring in Rush Springs based on high-resolution CASA data and damage signatures. As the RIJ impinged on the front-to-rear system-relative flow, it created an area of low- and midlevel convergence. The storm-relative motion and divergence cross sections in Fig. 18 suggest that momentum and convergence associated with the RIJ had been transported downward to enhance the pre-existing surface circulation. In Fig. 18d, the area of strong rotation at the surface (highlighted by the white oval) appears to be located just underneath the leading edge of the midlevel RIJ. Near the low-level velocity couplet, an area of strong convergence extends from ~1 to 4 km above MSL. These cross sections suggest that the Rush Springs mesovortex was enhanced by the downward transport of momentum and convergence associated with the strengthening RIJ.

6. COMPARISON TO KTLX AND TDWR-OKC

The QLCS was also sampled by KTLX, located ~20 km northeast of the PAR, and TDWR-OKC, located ~6 km northwest of the PAR (Fig. 1).

6.1 *Sampling strategies*

KTLX is an S-band (10-cm) radar with a beamwidth of ~0.89°. KTLX collects data with an azimuthal sampling interval of 0.5° at the two lowest elevation angles and has an effective beamwidth of ~1.02 as a result of antenna rotation (Brown et al. 2002). The KTLX range resolution is 250 m.

KTLX was operating continuously throughout the event and used two different scanning strategies. The first, Volume Coverage Pattern (VCP) 11, uses 14 elevation angles with a split cut waveform for the lowest two elevation angles (Brown et al. 2005). Around 1115 UTC, when the QLCS was located ~65 km from KTLX, the scanning strategy was switched to VCP 12 (Brown et al. 2005). VCP 12 also uses 14 elevation angles, but more elevation angles are focused on the lowest portion of the atmosphere. The volumetric update times for VCP 11 and 12 are 5 min and 4 min, respectively.

In contrast to KTLX and PAR, TDWR-OKC (hereafter TDWR) is a C-band (5-cm) radar and only provides Doppler velocity information out to 90 km in range. Thus, TDWR data are only available for the Rush Springs storm starting around 1100 UTC. Consequently, the majority of the radar comparisons in this paper will focus on PAR and KTLX.

TDWR has a beamwidth of 0.55°, but the azimuthal resolution is spoiled to 1° due to a lack of processing power. The TDWR range resolution is 150 m (NOAA 2005).

On 2 April 2010, TDWR was operating in hazardous mode, which is used when potentially severe storms are in range. Each hazardous mode scan consists of one long-range scan to properly place echoes in range and two volumetric scans (with elevation angles ranging from 0.5° to 28.2°). Scans at the 0.5° elevation angle are interlaced with the volumetric updates, so that data at the lowest elevation angle are available every 1 min. Each hazardous mode scan takes ~6 min (NOAA 2005).

6.2 *Microburst: PAR and KTLX*

PAR sampled the descending reflectivity core associated with the damage-producing microburst in great detail with five volumetric scans from 1037 UTC to 1048 UTC (Fig. 12). In contrast, KTLX only samples this process with three volumetric scans during this period (Fig. 19). As a result, the descent of the reflectivity core is only visible on one scan (Fig. 19b). By the next scan, the reflectivity core has already descended to the ground and is likely causing surface wind damage (Fig. 19c). This sampling limitation is also discussed in Heinselman et al. (2008) for another microburst event.

6.3 ***Rear-inflow jet: PAR and KTLX***

The RIJ was not well-sampled by KTLX, largely as a result of coarser vertical sampling. Fig. 20 compares interpolated and non-interpolated vertical cross sections from KTLX and PAR. The RIJ and lowest part of the storm were sampled at eight elevation angles in the 1052 UTC PAR scan, compared to only four elevation angles in the corresponding KTLX scan.

In the 1052 UTC cross section (Fig. 20d), the strongest region of the RIJ (storm-relative velocities exceeding 10 m s^{-1}) is visible in the PAR data near x~15 km, z~5 to 8.5 km. In contrast, the strongest part of the RIJ is only visible in the KTLX data near x~15 km, z~5.5 to 8 km (Fig. 20b); the RIJ core is shallower based on the coarser KTLX data. Since the RIJ was only sampled at three elevation angles by KTLX (Fig. 20a), it is more difficult to determine the full vertical extent of the RIJ based on the KTLX cross sections. In addition, the KTLX data required more interpolation to produce interpolated cross sections (e.g., Fig. 20b). For the KTLX data, interpolation was necessary to understand the vertical structure of the storm. In contrast, the interpolated and non-interpolated PAR cross sections are nearly identical.

6.4 ***Mesovortex circulation: PAR, KTLX, TDWR-OKC***

The velocity couplet was evident in the KTLX data, but the evolution of the azimuthal shear maximum was not depicted in great detail. Fig. 21 shows a KTLX azimuthal shear cross section taken along the path of the velocity couplet. Between 1052 and 1104 UTC, KTLX completed three full volume scans, compared to seven PAR volume scans in the same time period. While the PAR data show the circulation strengthen, grow in height, and subsequently weaken, the evolution is not as clear in the KTLX data. A time series of maximum low-level LLSD azimuthal shear values derived from the two radars (Fig. 22) further illustrates this point. Note that it is the trends in azimuthal shear, rather than the actual values, that are important in this case, since azimuthal shear values can vary according to range, radar angle, and beamwidth (Smith and Elmore 2004). The PAR data indicate a gradual increase in azimuthal shear from 1052 UTC to 1100 UTC, when the tornado was on the ground in Rush Springs, followed by a slight decrease and another increase at 1106 UTC as the circulation appears to re-intensify, possibly in response to the descending RIJ. The KTLX data do not show the evolution of these two azimuthal shear maxima.

Low temporal resolution could be a significant limitation for forecasters trying to issue warnings for a non-supercellular tornado. Since the circulation in this case appeared to form from the ground up, a descending circulation signature was not evident in radar data. Thus, by the time any evidence of rotation was apparent, the circulation was likely already causing damage on the ground.

Table 1 shows the maximum velocity difference associated with the circulation for all three radars at approximately the same times. The maximum velocity difference was defined as the absolute difference between the maximum and minimum storm-relative motion values at a constant range. Both the PAR and TDWR values show a similar trend — an increase at 1101 UTC, followed by a decrease in intensity. However, the TDWR velocity difference values are at least 4 m s^{-1} higher than the PAR values at all three scan times. In addition, the TDWR values all represent gate-to-gate velocity differences, while the PAR maximum and minimum velocities were separated by at least one azimuth. This discrepancy is likely due to the difference in beamwidth between TDWR and PAR. TDWR uses a 0.55° beamwidth with 150 m range resolution while the PAR beamwidth was ~1.6° at the circulation location with a 240 m range resolution. TDWR was likely sampling the small-scale, tornadic circulation while PAR was sampling the larger-scale, surrounding circulation. KTLX, with an effective beamwidth of ~1.02°, sampled similar velocity difference values to PAR.

7. SUMMARY AND CONCLUSIONS

The 2 April 2010 Oklahoma QLCS was examined using a variety of radar platforms. The NWRT PAR captured the evolution of the QLCS as damage equivalent to an EF1-scale tornado was occurring in Rush Springs, Oklahoma. High-resolution CASA data reveal the formation of a mesovortex along the leading edge of the QLCS, coincident with the tornado damage path (Mahale et al. 2010).

Around the time of mesovortex formation, PAR data show a bowing segment and intensifying rear-inflow jet. The rear-inflow jet impinged on the storm-relative front-to-rear flow, enhancing convergence along the gust front and likely promoting vertical stretching of the vorticity associated with the mesovortex. Analysis of the PAR azimuthal shear field shows a shear maximum grow in intensity and vertical extent before tilting downshear and weakening. Full volume scans were completed by the PAR every 2 min or less, revealing the evolution of these features in great detail. In addition, the PAR used an oversampled scanning strategy, collecting data at 22 elevation angles, compared to only 14 elevation angles used by the nearby WSR-88D radar in Twin Lakes, Oklahoma. The increased availability of volumetric PAR data ensured that the strengthening rear-inflow jet was well-resolved and observed in great detail. The PAR data also depict a descending reflectivity core associated with a microburst and the descent of the RIJ after formation of the mesovortex. Both these events occurred on very short time scales (5 min or less) and were therefore not depicted in great detail by KTLX.

The evolution of the Rush Springs circulation is summarized in Fig. 23. As observed in the PAR data, the RIJ began to strengthen at 1049 UTC, possibly providing the low-altitude convergence necessary to strengthen the pre-existing mesovortex and promote tornadogenesis. Less than 10 min after the strengthening RIJ was first seen in the PAR data, a surface circulation formed and began causing damage in Rush Springs. The entire process, from the start of the RIJ forcing to the end of the wind damage associated with the circulation, took place in just under 15 min. The rapid evolution of this event highlights the importance of having high-temporal-resolution data to depict trends in potentially tornadic storms.

QLCS tornadoes account for nearly 20% of all tornadoes and frequently occur during the late night and early morning hours, when the public is less aware of severe weather hazards (Trapp et al. 1999). The 2 April 2010 Rush Springs event reveals that significant changes can occur in quasi-linear convective systems on very short times scales. Monitoring midlevel features, such as the rear-inflow jet, requires a vast amount of volumetric data not available with the current WSR-88D network. In the future, more high-temporal-resolution data collected on QLCS cases could further advance the knowledge of mesovortex formation and highlight radar precursors for QLCS tornadoes.

8. ACKNOWLEDGMENTS

The authors thank Rick Hluchan for monitoring PAR data collection on the day of the event, Kevin Manross for assisting with acquisition of TDWR data, Kiel Ortega for supplying damage survey information, and Jeff Brogden for assisting with PAR data conversion. The authors would also like to acknowledge the developers of NCAR's Soloii radar data editing program and Dennis Flanigan, the developer of the PAR data translator for Soloii. Funding for the first author was provided under NOAA-OU Cooperative Agreement NA17RJ1227.

9. REFERENCES

Ashley, W. S., A. J. Krmenec, and R. Schwantes, 2008: Vulnerability due to nocturnal tornadoes. *Wea. Forecasting*, **23,** 795–807.

Atkins, N. T., C. S. Bouchard, R. W. Przybylinski, R. J. Trapp, and G. Schmocker, 2005: Damaging surface wind mechanisms within the 10 June 2003 Saint Louis bow echo during BAMEX. *Mon. Wea. Rev.*, **133**, 2275–2296.

Atkins, N. T., and M. St. Laurent, 2009a: Bow echo mesovortices. Part I: Processes that influence their damaging potential. *Mon. Wea. Rev.*, **137,** 1497–1513.

Atkins, N. T., and M. St. Laurent, 2009b: Bow echo mesovortices. Part II: Their genesis. *Mon. Wea. Rev.*, **137**, 1514–1532.

Brown, R. A., L. R. Lemon, and D. W. Burgess, 1978: Tornado detection by pulsed Doppler radar. *Mon. Wea. Rev.,* **106,** 29–39.

Brown, R. A., V. T. Wood, and D. Sirmans, 2002: Improved tornado detection using simulated and actual WSR-88D data with enhanced resolution. *J. Atmos. Oceanic Technol*., **19**, 1759–1771.

Brown, R. A., V. T. Wood, R .M. Steadham, R. R. Lee, B. A. Flickinger, and D. Sirmans, 2005: New WSR-88D volume coverage pattern 12: Results of field tests. *Wea. Forecasting*, **20,** 385–393.

Doswell, C. A., 2001: Severe convective storms — An overview. *Severe Convective Storms, Meteor. Monogr.,* No. 50, Amer. Meteor. Soc., 1–26.

Evans, J. S., and C. A. Doswell, 2001: Examination of derecho environments using proximity soundings. *Wea. Forecasting*, **16**, 329–342.

Forbes, G. S., and R. M. Wakimoto, 1983: A concentrated outbreak of tornadoes, downbursts and microbursts, and implications regarding vortex classification. *Mon. Wea. Rev.*, **111**, 220–236.

Fujita, T. T., 1971: Proposed characterization of tornadoes and hurricanes by area and intensity. SMRP Res. Paper No. 91, The Univ. of Chicago, Chicago, IL, 42 pp.

Fujita, T. T., 1978: Manual of downburst identification for Project NIMROD. SMRP Res. Paper No.156, The Univ. of Chicago, Chicago, IL, 104 pp.

Fujita, T. T., 1981: Tornadoes and downbursts in the context of generalized planetary scales. *J. Atmos. Sci.*, **38**, 1511–1534.

Heinselman, P. L., D. L. Priegnitz, K. L. Manross, T. M. Smith, and R. W. Adams, 2008: Rapid sampling of severe storms by the National Weather Radar Testbed Phased Array Radar. *Wea. Forecasting*, **23,** 808–824.

Heinselman, P. L., and S. M. Torres, 2010: High-temporal resolution capabilities of the National Weather Radar Testbed Phased-Array Radar. *J. Appl. Meteor. Climatol*., in press.

Junyent, F., V. Chandrasekar, D. McLaughlin, E. Insanic, and N. Bharadwaj, 2010: The CASA Integrated Project 1 networked radar system. *J. Atmos. Oceanic Technol.*, **27**, 61–78.

Maddox, R. A., 1983: Large scale meteorological conditions associated with midlatitude mesoscale convective complexes. *Mon. Wea. Rev.*, **111**, 1475–1493.

Mahale, V. N., J. Brotzge, and H. B. Bluestein, 2010: The detection of low-level misovortices embedded within a quasi-linear thunderstorm complex on 2 April 2010 by CASA radar. Preprints, *25th Conf. on Severe Local Storms*, Denver, CO, Amer. Meteor. Soc., 4A.5.

Markowski, P. M., and Y. P. Richardson, 2010: *Mesoscale Meteorology in Midlatitudes*. Wiley, 407 pp.

Marshall, T. P., 2004: The enhanced Fujita (EF) scale. Preprints, *22nd Conf. on Severe Local Storms,* Hyannis, MA, Amer. Meteor. Soc., 3B.2.

NCDC 2010: *Storm Data.* Vol. 52, No. 4, 384 pp.

NOAA, NWS, and OSTSEC, 2005: TDWR interface control and specifications documentation for the NWS supplemental product generator. Technical report, National Oceanic and Atmospheric Administration.

Smith, T. M., and K. L. Elmore, 2004: The use of radial velocity derivatives to diagnose rotation and divergence. Preprints, *11th Conf. on Aviation, Range, and Aerospace,* Hyannis, MA, Amer. Meteor. Soc., P5.6.

Smull, B. F., and R. A. Houze Jr., 1987: Rear inflow in squall lines with trailing stratiform precipitation. *Mon. Wea. Rev.* **115**, 2869–2889.

Trapp, R. J., E. D. Mitchell, G. A. Tipton, D. W. Effertz, A. I. Watson, D. L. Andra, and M. A. Magsig, 1999: Descending and nondescending tornadic vortex signatures detected by WSR-88Ds. *Wea. Forecasting*, **14**, 625–639.

Trapp, R. J., and M. L. Weisman, 2003: Low-level mesovortices within squall lines and bow echoes. Part II: Their genesis and implications. *Mon. Wea. Rev.*, **131**, 2804–2823.

Trapp, R. J., S. A. Tessendorf, E. S. Godfrey, and H. E. Brooks, 2005: Tornadoes from squall lines and bow echoes. Part I: Climatological distribution. *Wea. Forecasting*, **20**, 23–34.

Wakimoto, R. M., and J. W. Wilson, 1989: Non-supercell tornadoes. *Mon. Wea. Rev.*, **117**, 1113–1140.

Wakimoto, R. M., H. V. Murphey, A. Nester, D. P. Jorgensen, and N. T. Atkins, 2006a: High winds generated by bow echoes. Part I: Overview of the Omaha bow echo 5 July 2003 storm during BAMEX. *Mon. Wea. Rev.*, **134**, 2793–2812.

Wakimoto, R. M., H. V. Murphey, C. A. Davis, and N. T. Atkins, 2006b: High winds generated by bow echoes. Part II: The relationship between the mesovortices and damaging straight-line winds. *Mon. Wea. Rev.*, **134**, 2813–2829.

Weisman, M. L., 1993: The genesis of severe, long-lived bow echoes. *J. Atmos. Sci.*, **50**, 645–670.

Weisman, M. L., and R. J. Trapp, 2003: Low-level mesovortices within squall lines and bow echoes. Part I: Overview and sensitivity to environmental vertical wind shear. *Mon. Wea. Rev.*, **131**, 2779–2803.

Wheatley, D. M., R. J. Trapp, and N. T. Atkins, 2006: Radar and damage analysis of severe bow echoes observed during BAMEX. *Mon. Wea. Rev.*, **134**, 791–806.

Zrnić, D. S., and Coauthors, 2007: Agile-beam phased array radar for weather observations. *Bull. Amer. Meteor. Soc.*, **88**, 1753–1766.

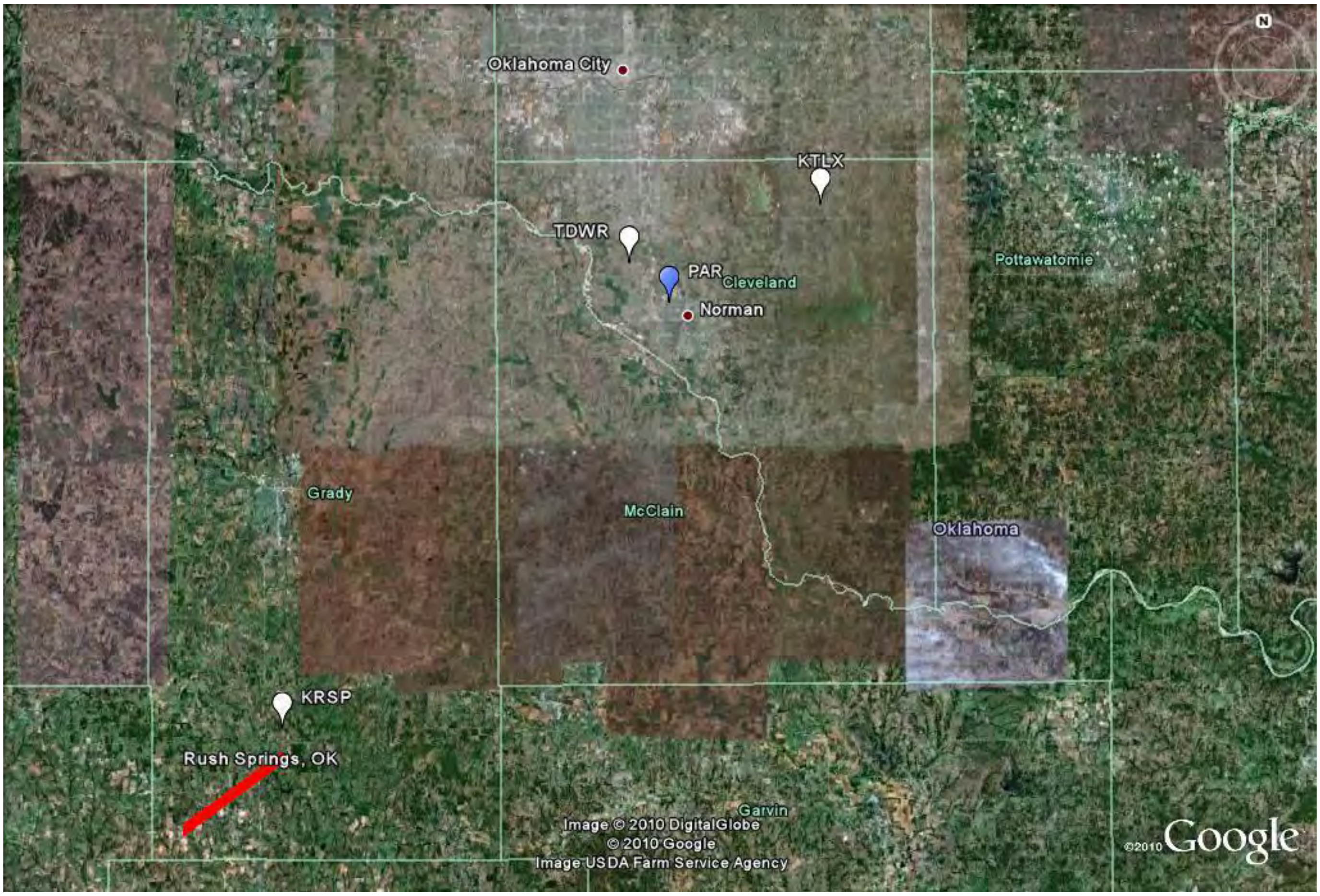

Fig. 1. Location of central Oklahoma radars discussed in the text. Path of Rush Springs tornado shown in red.

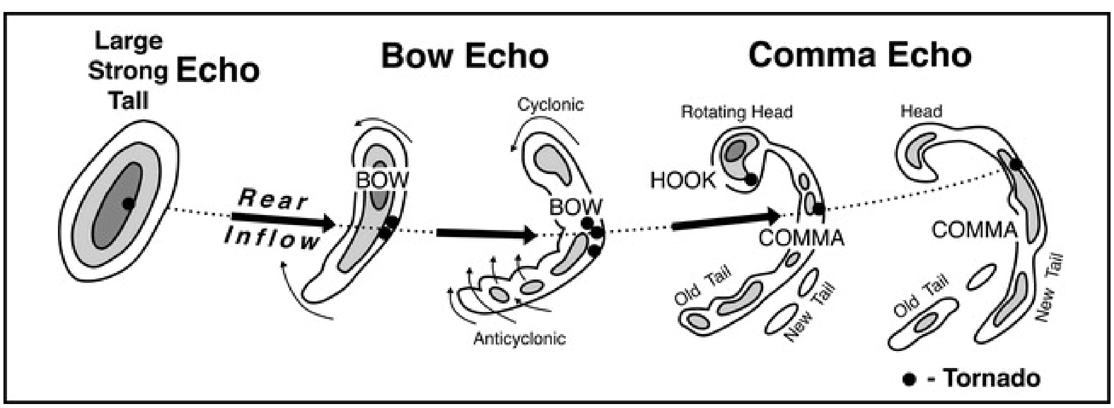

Fig. 2. Conceptual model of the life cycle of a bow echo. Black circles indicate tornado locations. Black arrows indicate location of the rear-inflow jet. From Wakimoto et al. (2006a). Originally adapted from Fujita (1978).

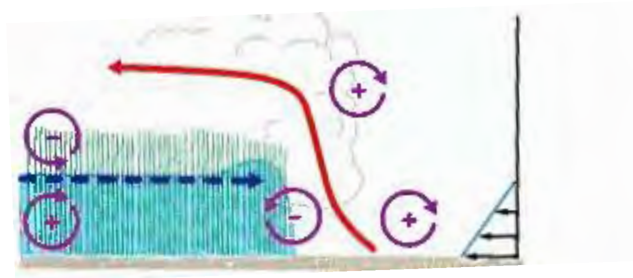

Fig. 3. Final stage in the formation of an idealized bow echo. Purple arrows indicate the sense of environmental and baroclinic vorticity. Black lines indicate environmental vertical wind shear. Green lines indicate precipitation and blue area indicates cold pool. Red line denotes front-to-rear flow and blue dotted line denotes rear-to-front inflow. From Markowski and Richardson (2010). Adapted from Weisman (1993).

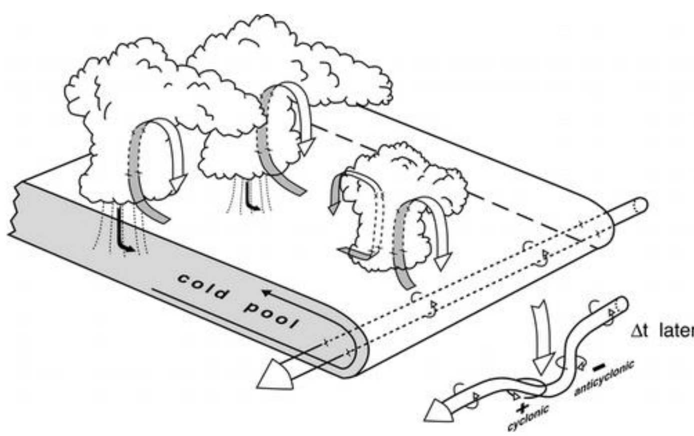

Fig. 4. Conceptual model of mesovortex generation along outflow boundary of 5 July 2003 Omaha bow echo. The vortex tube in the bottom right shows how a downdraft tilted baroclincally generated vorticity, forming a vertical vorticity couplet. From Wakimoto et al. (2006b).

a)

b)

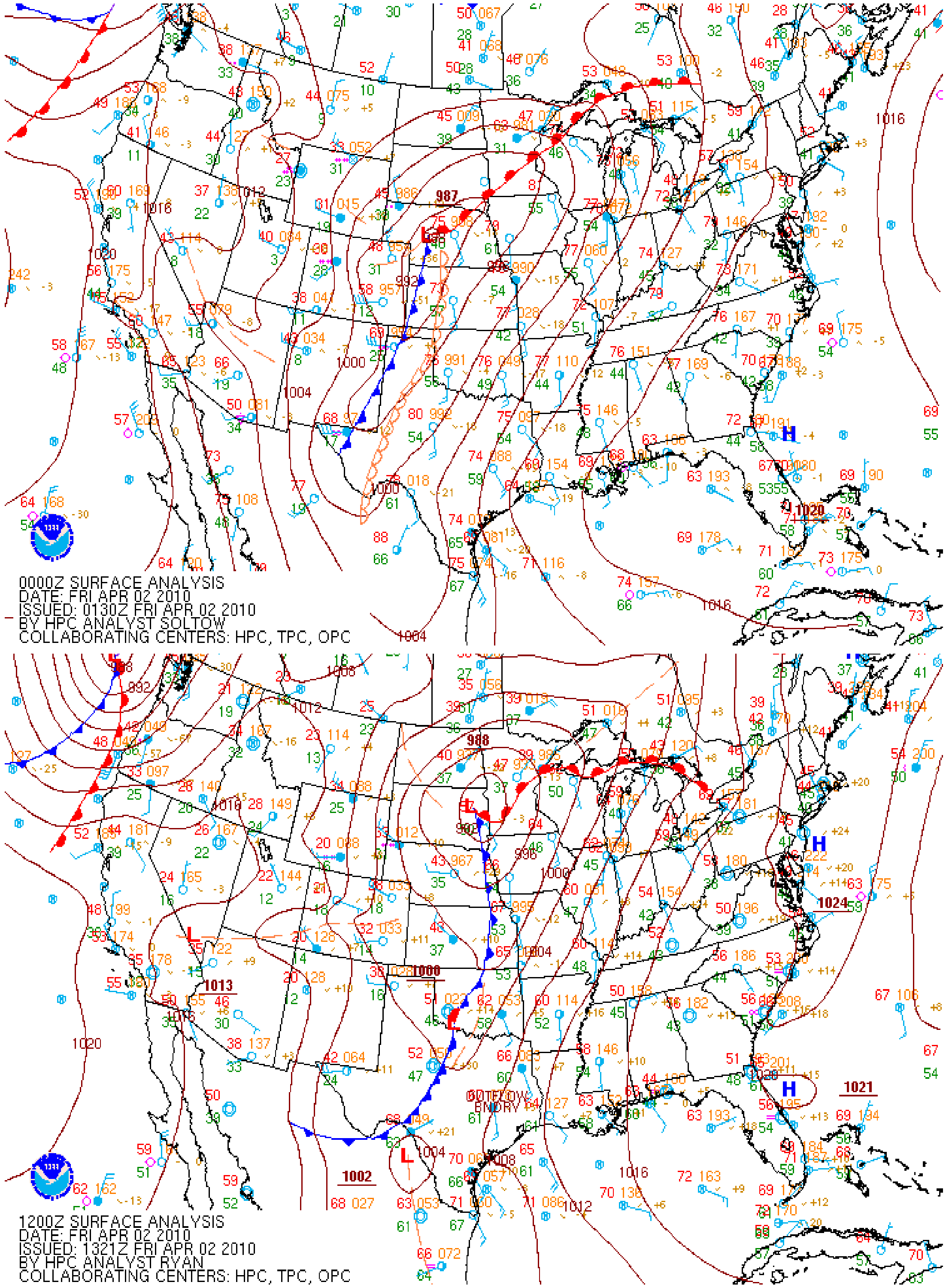

Fig. 5. NCEP surface analyses on 2 April 2010. Station plots show temperature (red numbers, in °F), dewpoint temperature (green numbers, in °F), sea-level pressure (yellow numbers, in tenths of hPa with leading 10 or 9 omitted), and wind (blue barbs, with one barb equal to ten kts and one pennant equal to 50 kts). Isobars are plotted in red (increments of 4 hPa) and standard frontal symbols are used. a) 0000 UTC 2 April 2010 b) 1200 UTC 2 April 2010.

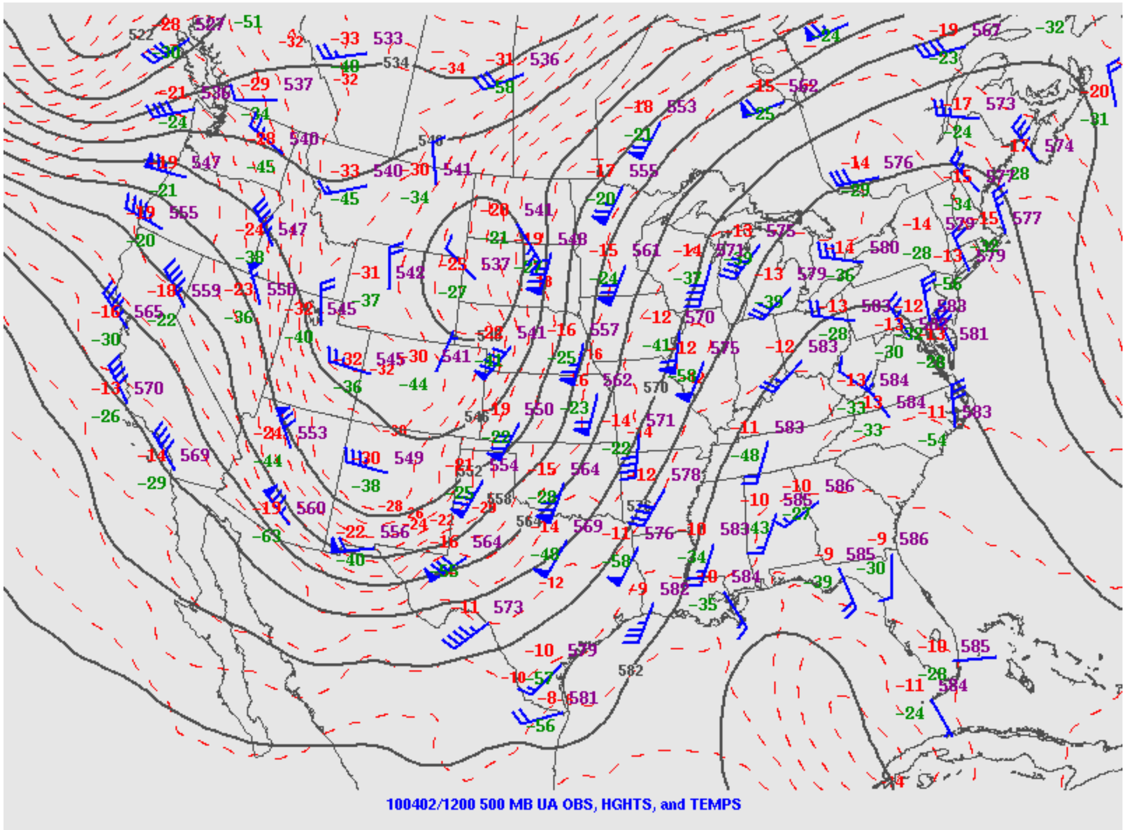

Fig. 6. 1200 UTC 2 April 2010 500-hPa chart from the Storm Prediction Center. Station plots show temperature (red numbers, in °C), dewpoint temperature (green numbers, in °C), height (purple numbers, in meters, with final 0 omitted), and wind (blue barbs, with one barb equal to ten kts and one pennant equal to 50 kts). 500-hPa heights (gray lines, with final 0 omitted, in 600 m increments) and isotherms (red dashed lines, in 1 °C increments) are also plotted.

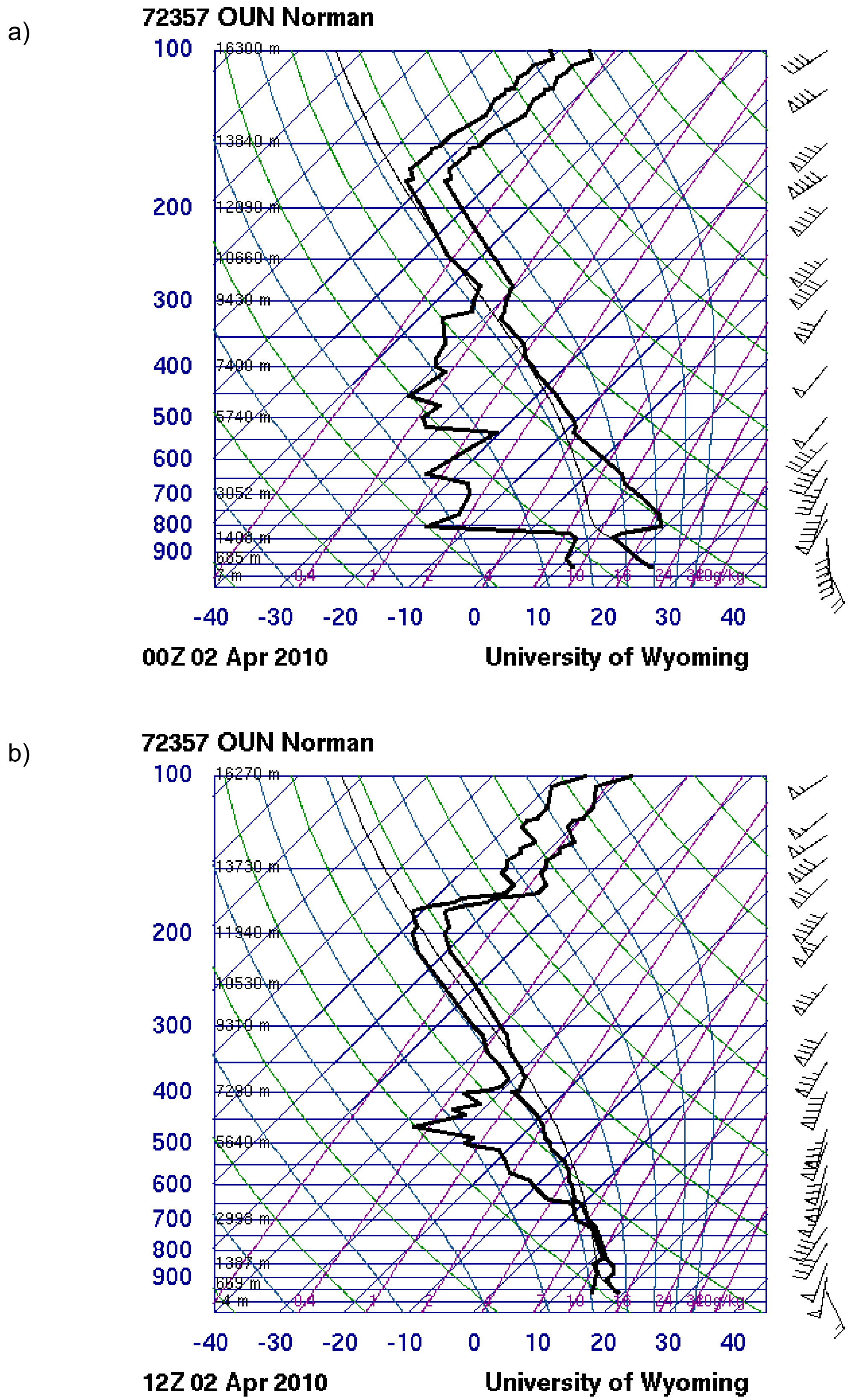

Fig. 7. Soundings from a) 0000 UTC and b) 1200 UTC on 2 April 2010 from Norman, OK. Pressure is plotted in hPa and temperature is plotted in °C. Wind barbs are shown in units of m s^{-1}, with one whole barb equal to 5 m s^{-1} and one pennant equal to 25 m s^{-1}.

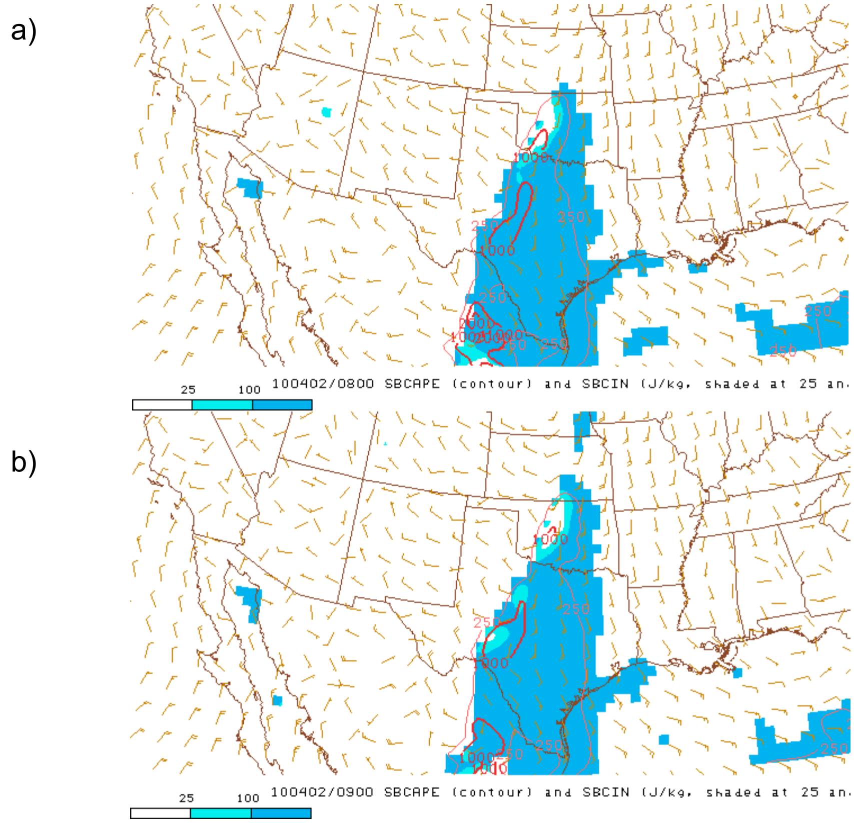

Fig. 8. a) 0800 UTC and b) 0900 UTC SPC mesoanalyses from 2 April 2010. Surface-based CAPE is contoured in intervals of 25 J kg^{-1}. Surface-based convective inhibition (CIN) is shaded as indicated.

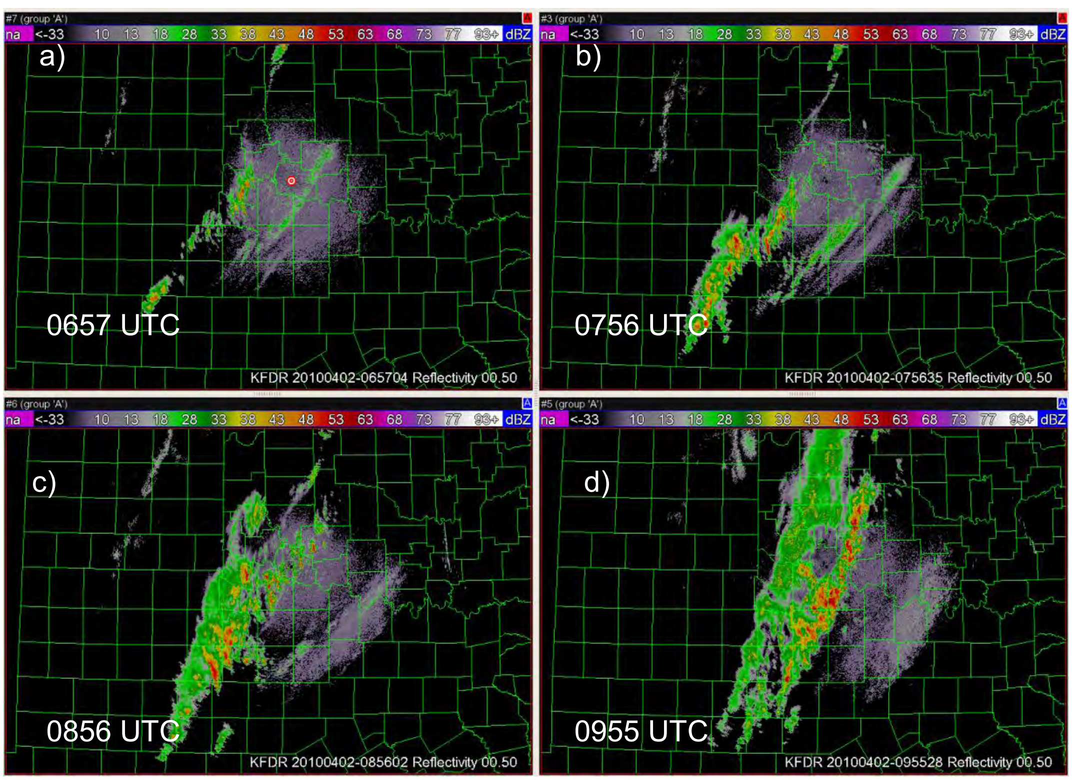

Fig. 9. The 0.5° reflectivity from the WSR-88D radar in Frederick, Oklahoma. Oklahoma and Texas counties are outlined in green. Red and white marker in first image shows radar location. a) 0657 UTC b) 0756 UTC c) 0856 UTC d) 0955 UTC.

a)

b)

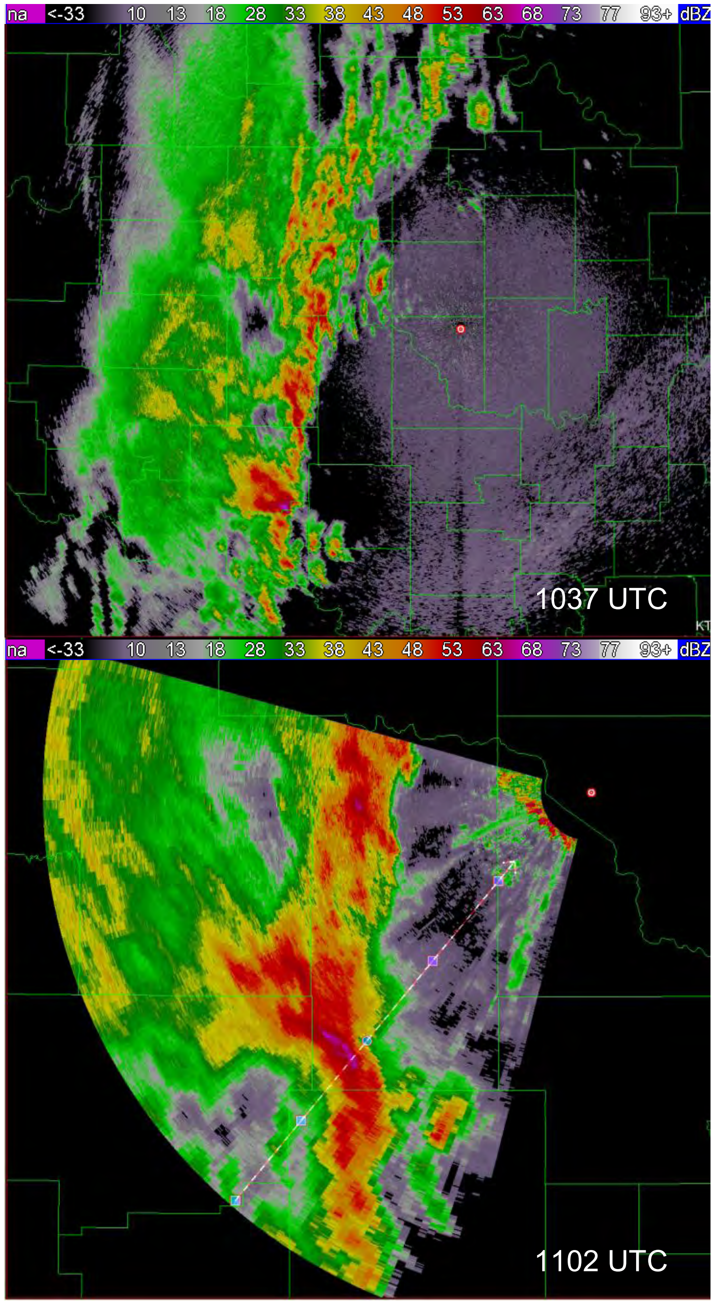

Fig. 10. a) KTLX 0.5° reflectivity at 1037 UTC on 2 April 2010. b) PAR 0.5° reflectivity at 1102 UTC on 2 April 2010. Dotted line shows cross section location discussed in PAR analysis section. In both images, Oklahoma counties are outlined in green, and red and white marker shows radar location.

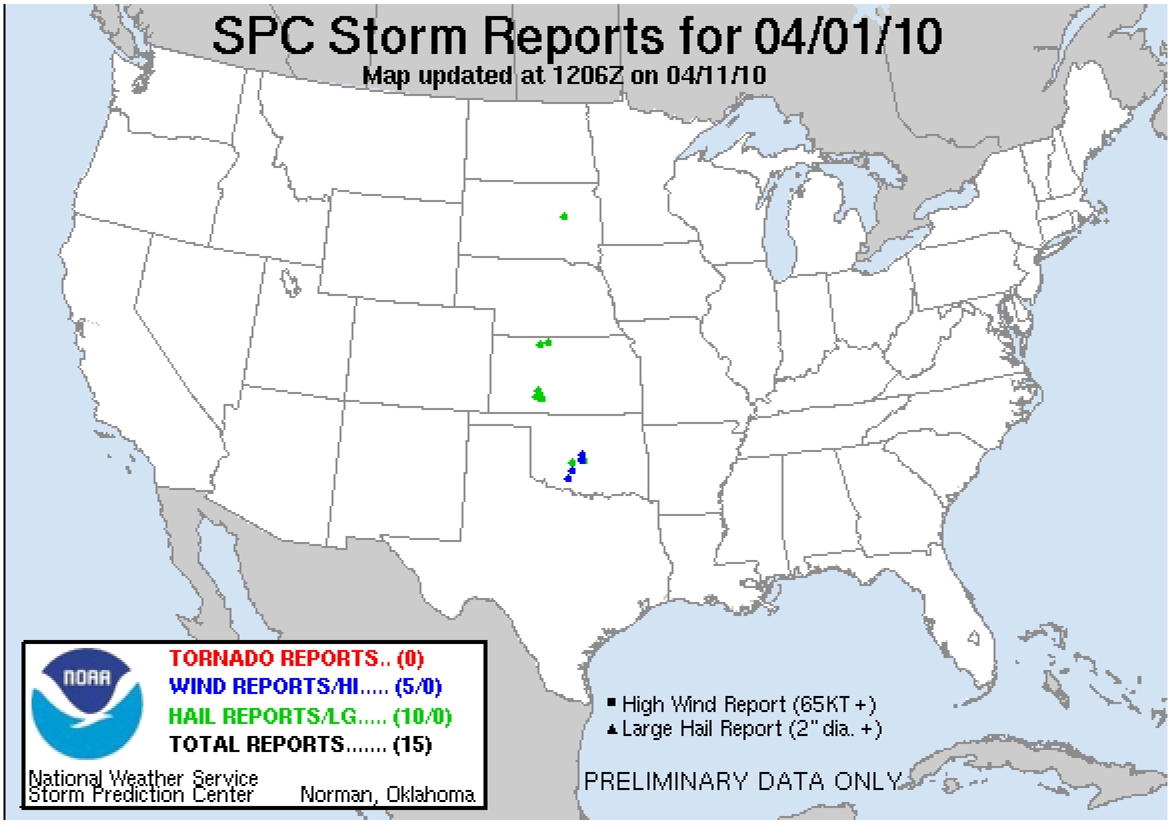

Fig. 11. SPC storm reports for 1200 UTC 1 April 2010 to 1200 UTC 2 April 2010.

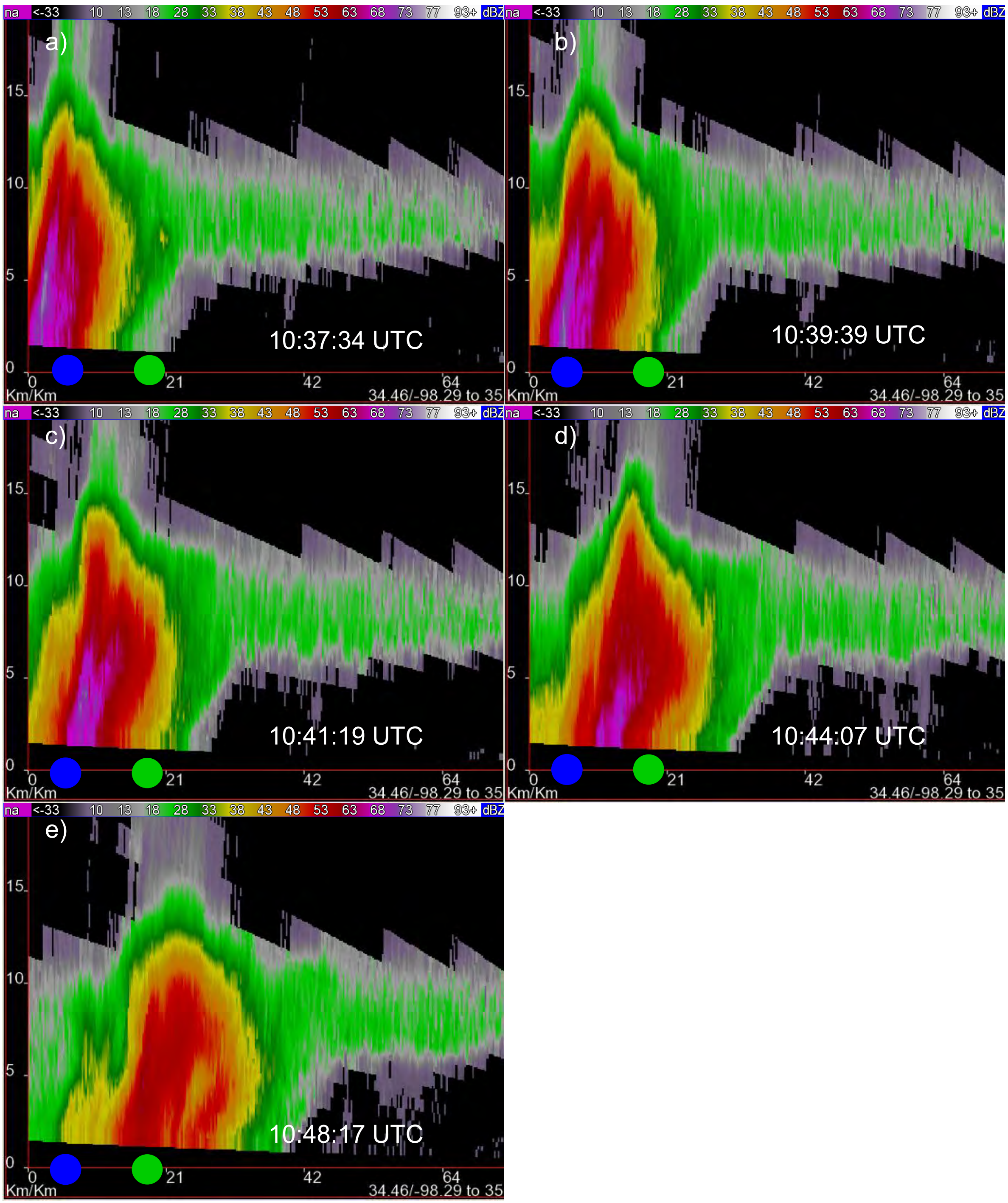

Fig. 12. PAR northeast-southwest reflectivity cross section. Location of cross section shown in Fig. 10. Increasing numbers on the x-axis indicate decreasing distance from PAR. Reflectivity units are dBZ. Blue and green circles denote approximate locations of wind and hail reports, respectively, as discussed in the text. At 1037 UTC, the southern portion of the QLCS was located ~113 km from PAR. a) 10:37:34 UTC b) 10:39:39 UTC c) 10:41:19 UTC d) 10:44:07 UTC e) 10:48:17 UTC.

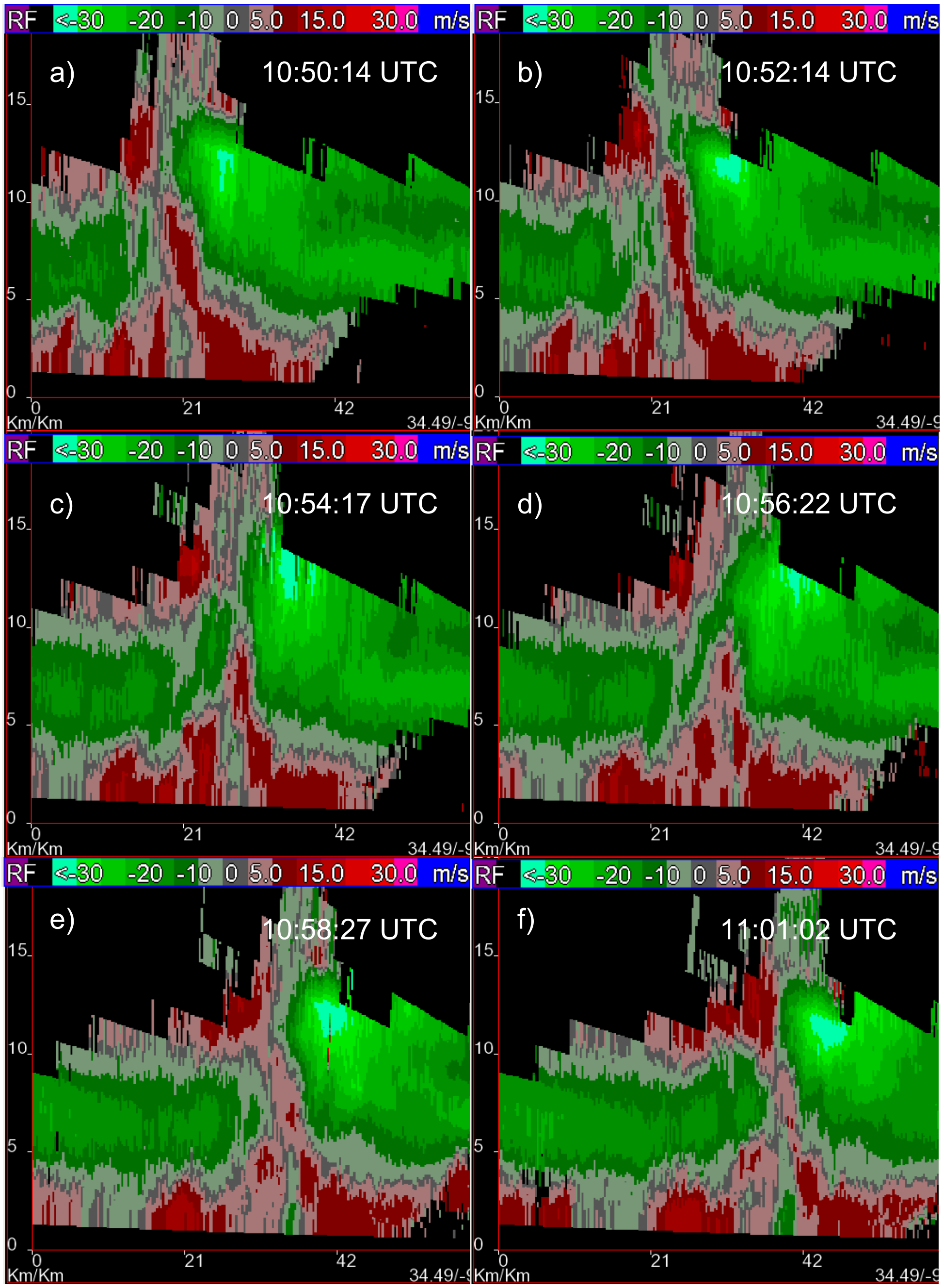

Fig. 13. PAR northeast-southwest storm-relative motion cross section. Location of cross section shown in Fig. 10. Increasing numbers on the x-axis indicate decreasing distance from the PAR. Velocity units are m s^{-1}. (Storm motion was determined by using an algorithm that tracks the low-level reflectivity field.) At 1050 UTC, the QLCS was located ~95 km from the PAR. a) 10:50:14 UTC b) 10:52:14 UTC c) 10:54:17 UTC d) 10:56:22 UTC e) 10:58:27 UTC f) 11:01:02 UTC.

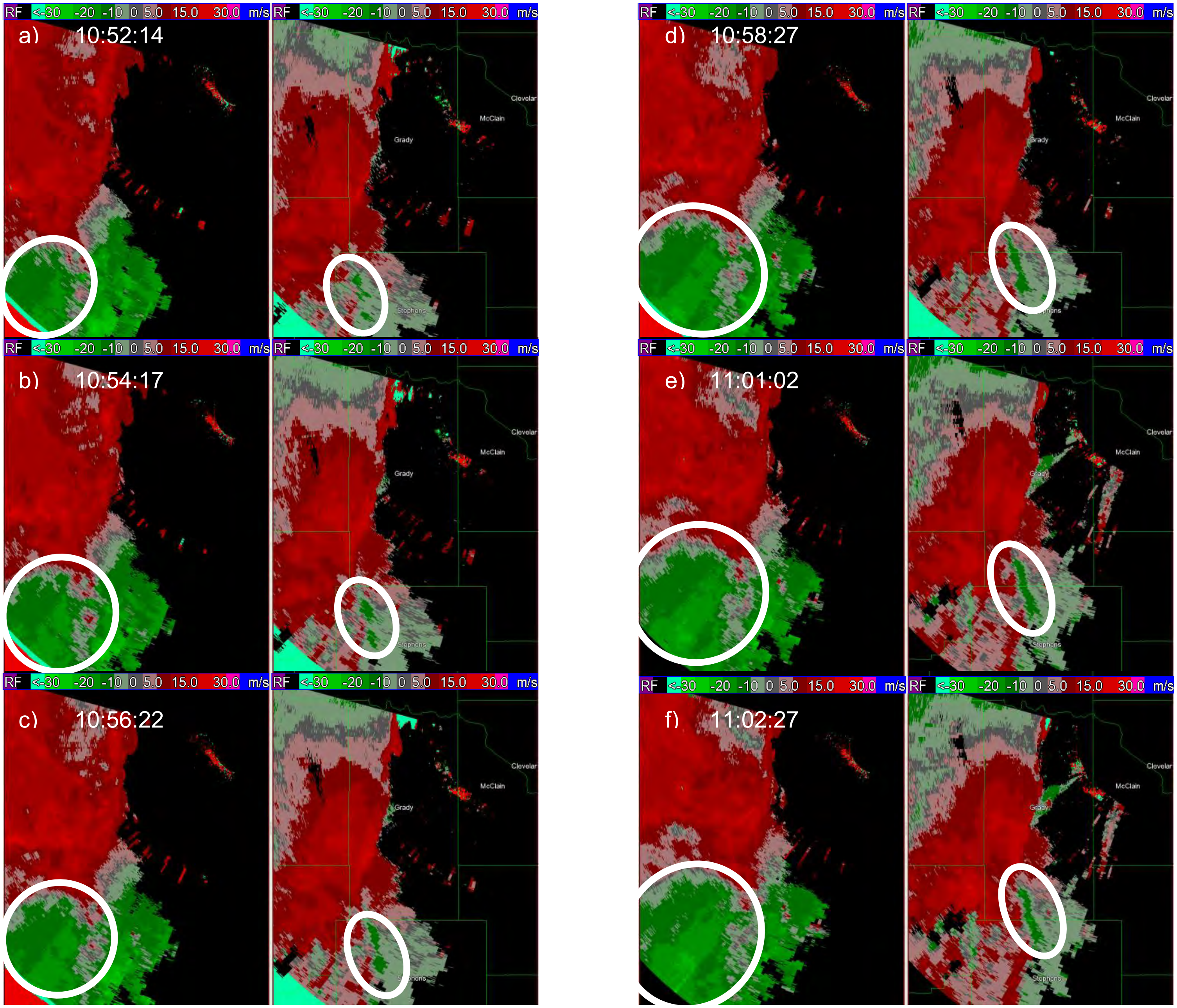

Fig. 14. PAR 3.07° (left) and 0.5° (right) storm-relative motion PPI scans at a) 10:52:14 UTC b) 10:54:17 UTC c) 10:56:22 UTC d) 10:58:27 UTC e) 11:01:02 UTC f) 11:02:27 UTC. PAR is located in upper right corner of images. White circles in 3.07° and 0.5° images highlight strengthening RIJ and strengthening near-surface outflow, respectively. Oklahoma counties are outlined in green in 0.5° velocity images. Note developing velocity couplet at northeastern edge of 0.5° outflow. At 1052 UTC, the northeastern edge of the surface outflow was located ~85 km from the PAR; the 0.5° and 3.07° scans were sampling the atmosphere at 1.6 and 5.5 km above MSL, respectively.

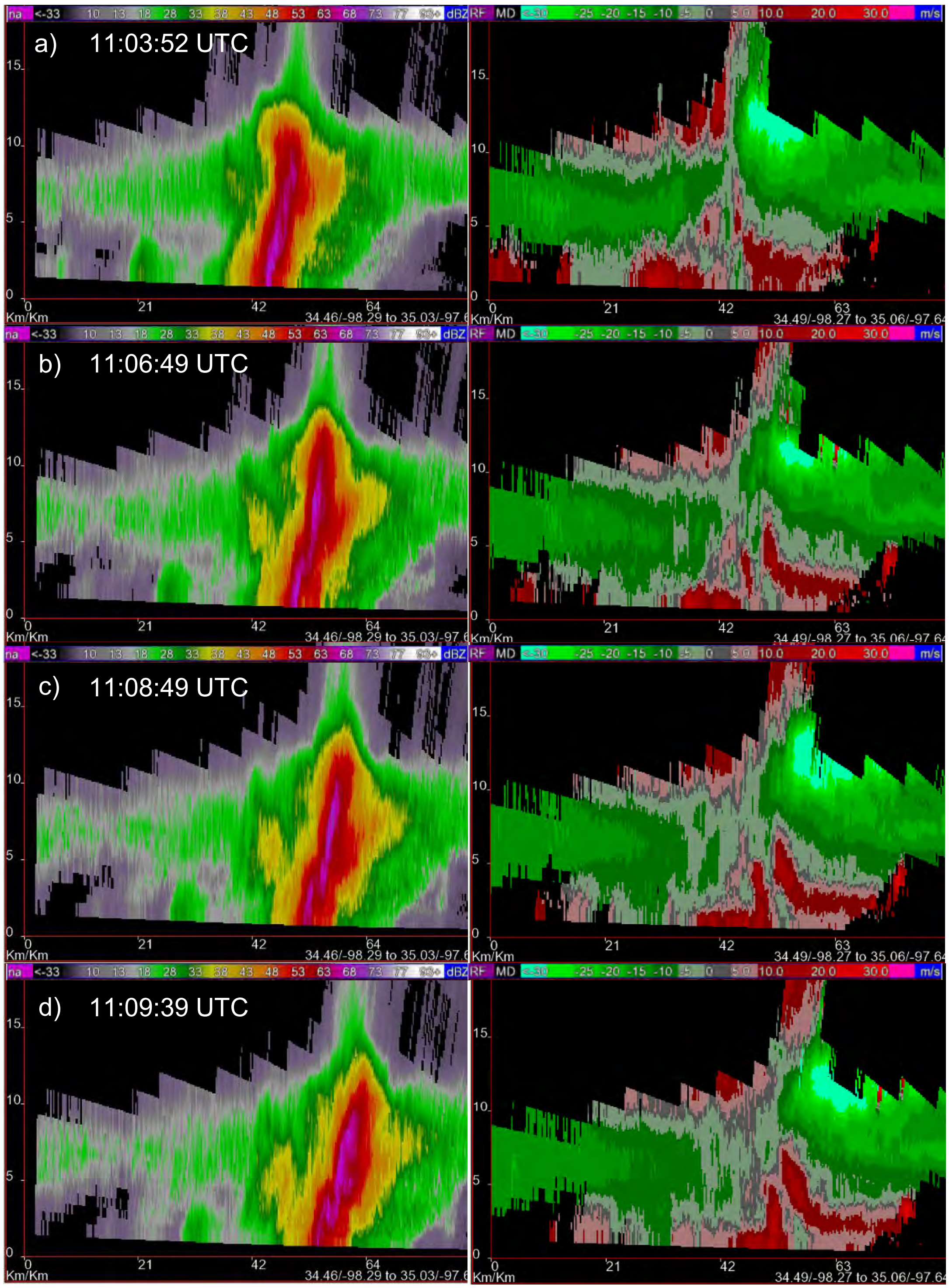

Fig. 15. PAR northeast-southwest oriented cross section. Location of cross section shown in Fig. 10. Increasing numbers on the x-axis indicate decreasing distance from the PAR. Reflectivity (left) units are dBZ; storm-relative motion (right) units are m s^{-1}. At 1103 UTC, the QLCS was located ~70 km from the PAR. a) 11:03:52 UTC b) 11:06:49 UTC c) 11:08:49 UTC d) 11:09:39 UTC.

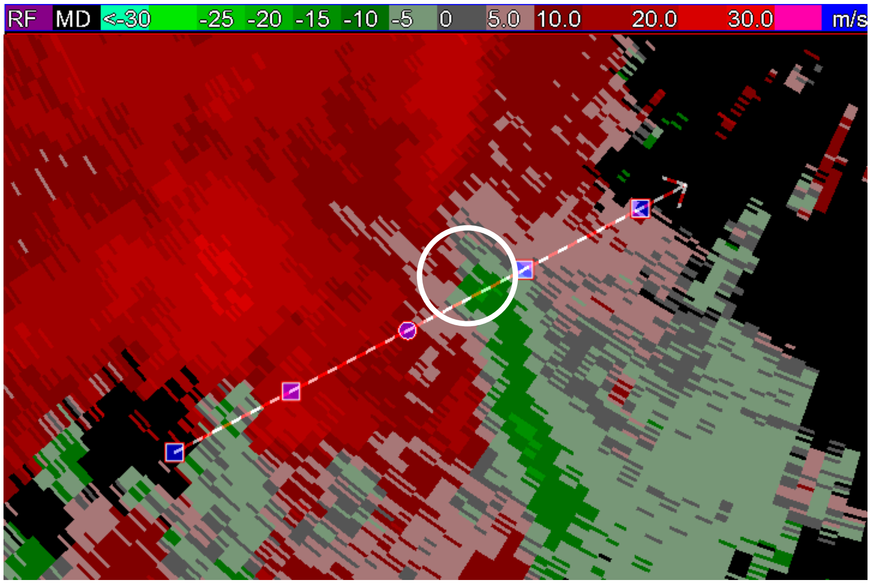

Fig. 16. PAR 0.5° storm-relative motion at 11:02:27 UTC. Dashed line shows location of cross sections in Figs. 17 and 18. White circle indicates location of velocity couplet associated with Rush Springs circulation. At 1102 UTC, the circulation was located 68 km from the PAR.

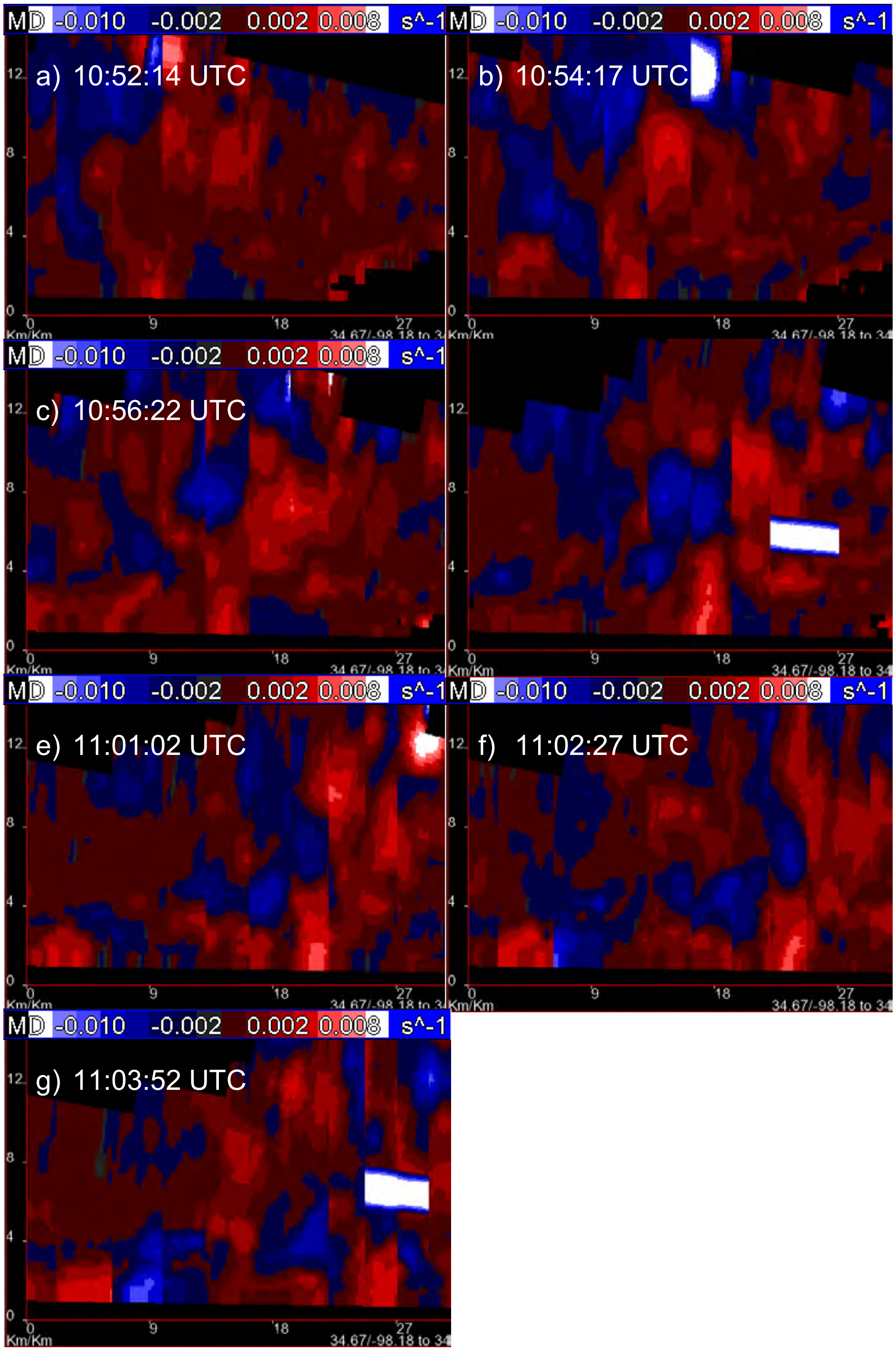

Fig. 17. PAR northeast-southwest oriented cross section. Location of cross section shown in Fig. 16. Increasing numbers on the x-axis indicate decreasing distance from the PAR. Azimuthal shear units are s^{-1}. White oval indicates location of azimuthal shear associated with circulation. At 1052 UTC, the circulation was located 86 km from the PAR. a) 10:52:14 UTC b) 10:54:17 UTC c) 10:56:22 UTC d) 10:58:27 UTC e) 11:01:02 UTC f) 11:02:27 UTC g) 11:03:52 UTC.

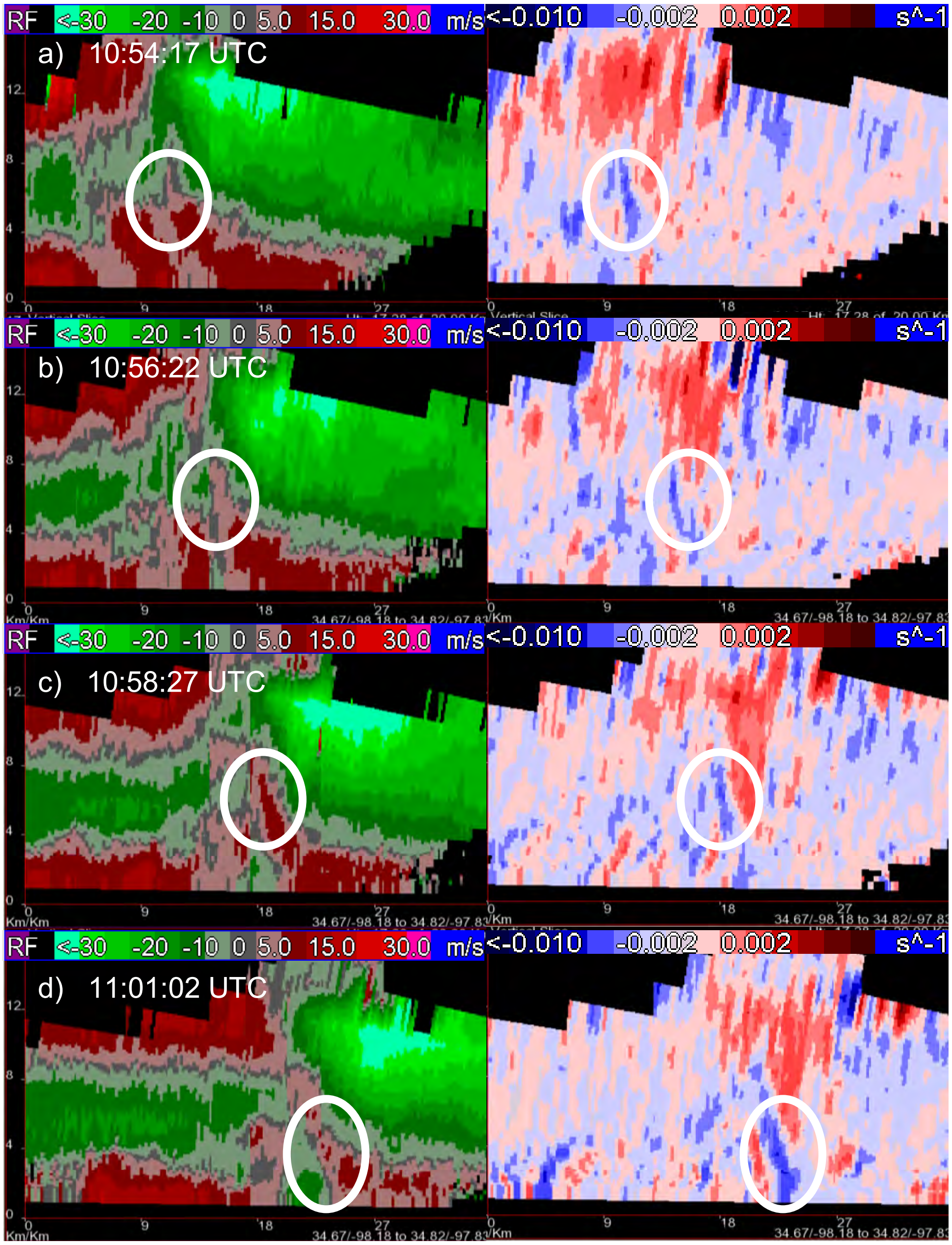

Fig.18. PAR northeast-southwest oriented storm-relative motion (left) and divergence (right) cross sections. Location of cross section shown in Fig. 16. Increasing numbers on the x-axis indicate decreasing distance from the PAR. At 1054 UTC, the circulation was located 82 km from the PAR. Divergence was calculated using the LLSD method (Smith and Elmore 2004). Area of convergence associated with RIJ is indicated by white oval. a) 10:54:17 UTC b) 10:56:22 UTC c) 10:58:27 UTC d) 11:01:02 UTC.

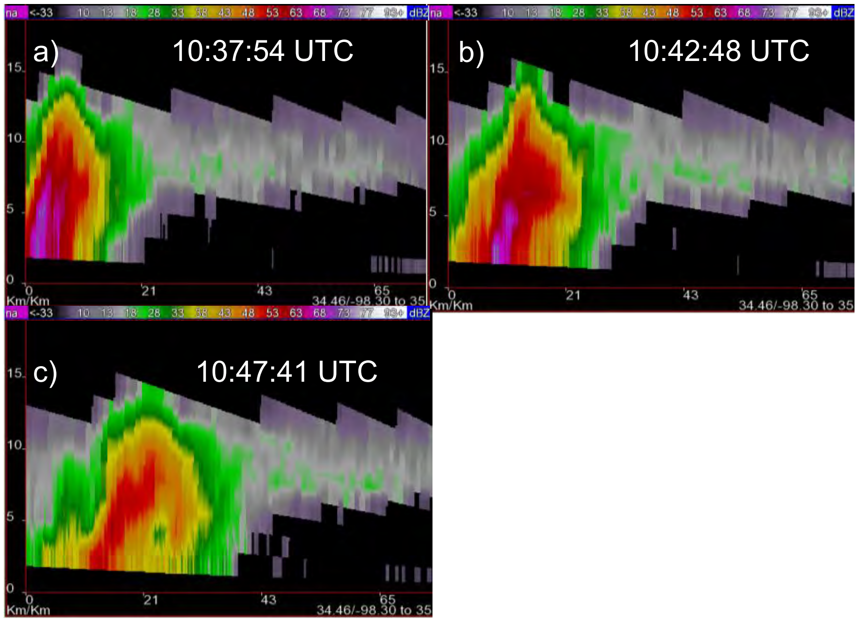

Fig. 19. KTLX northeast-southwest reflectivity cross section. Location of cross section shown in Fig. 10. Increasing numbers on the x-axis indicate decreasing distance from KTLX. Reflectivity units are dBZ. At 1037 UTC, the southern portion of the QLCS was located ~130 km from KTLX. a) 10:37:54 UTC b) 10:42:48 UTC c) 10:47:41 UTC.

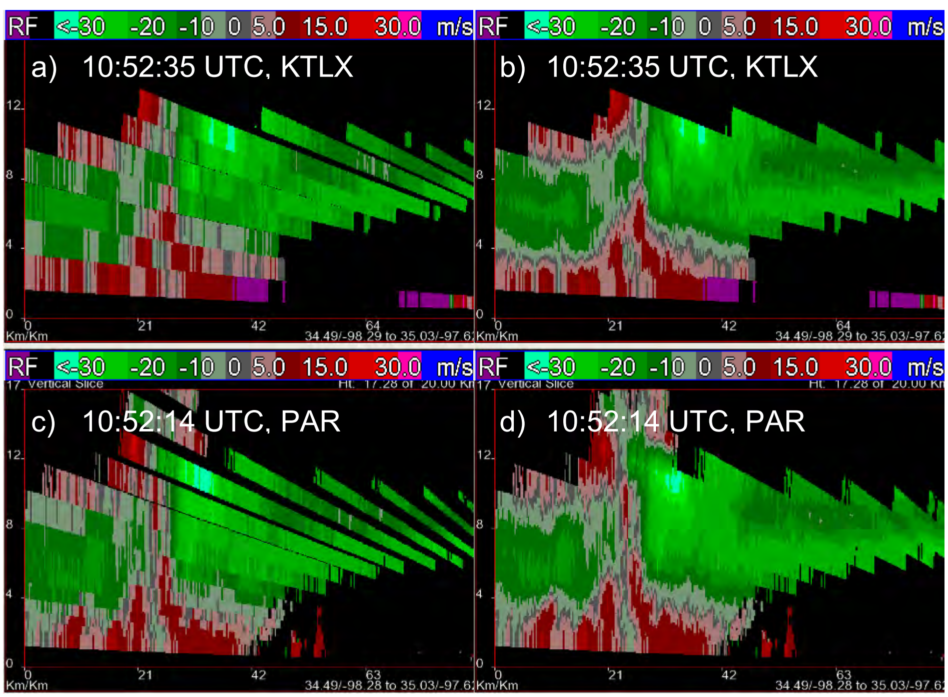

Fig. 20. KTLX and PAR northeast-southwest storm-relative motion cross sections. Location of cross section shown in Fig. 10. Increasing numbers on the x-axis indicate decreasing distance from the radars. At 1052 UTC, the QLCS was located ~86 km from the PAR and ~106 km from KTLX. Velocity units are m s^{-1}. Times refer to time of 0.5° elevation scan. a) KTLX, 10:52:35 UTC, non-interpolated b) KTLX, 10:52:35 UTC, interpolated c) PAR, 10:52:14 UTC, non-interpolated d) PAR, 10:52:14 UTC, interpolated.

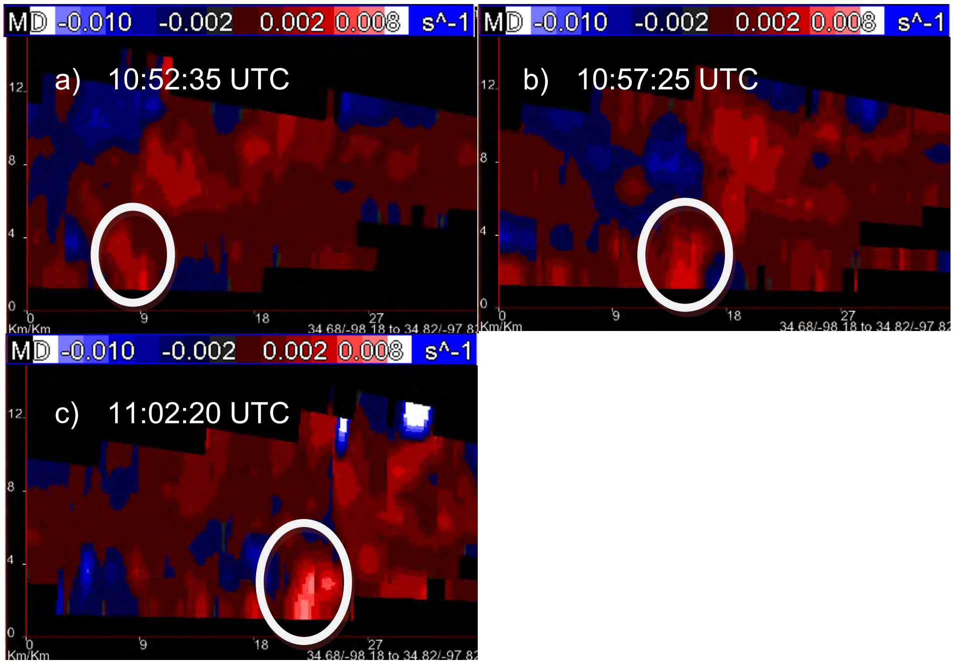

Fig. 21. As in Fig. 17, but for KTLX azimuthal shear. At 1052 UTC, the circulation was located ~106 km from KTLX. a) 10:52:35 UTC b) 10:57:25 c) 11:02:20 UTC.

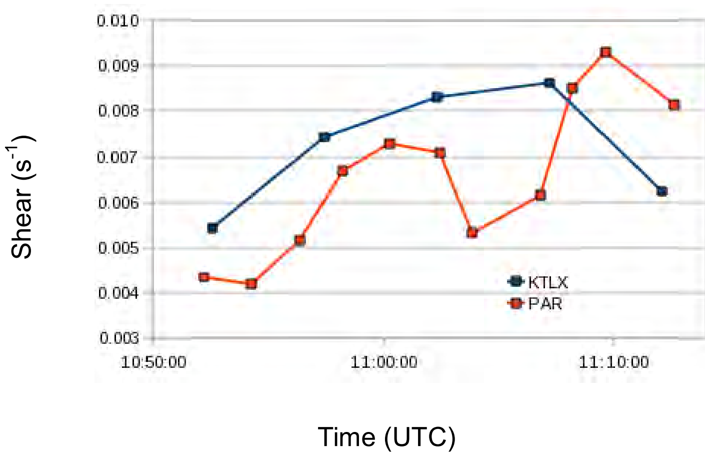

Fig. 22. Time series of maximum 0.5° azimuthal shear values associated with circulation from KTLX (blue line) and PAR (red line).

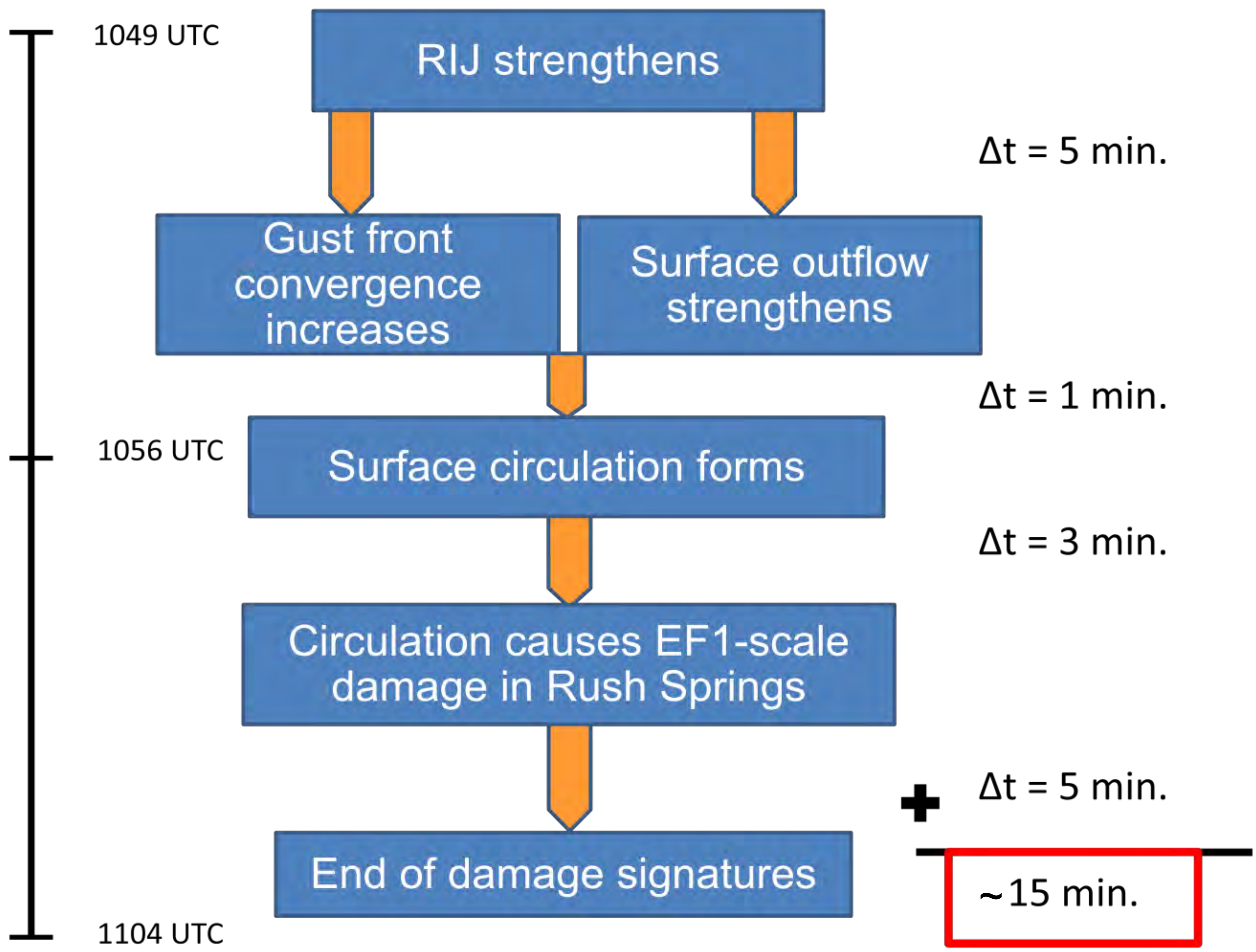

Fig. 23. Diagram depicting evolution of Rush Springs circulation as observed in PAR data. Time increases toward the bottom of the diagram. Δt is the time elapsed between the start times of subsequent radar-indicated signatures.

	PAR	KTLX	TDWR
Approximate time			
1058 UTC	18	19	23.5
1101 UTC	21.5	-	26
1103 UTC	20.5	19	24.5

Table 1. Comparison of maximum velocity difference (in m s^{-1}) for all three radars.